ROYAL SOCIETY OF CHEMISTRY

EDGE ARTICLE

Check for updates

All publication charges for this article have been paid for by the Royal Society of Chemistry

Sulfur oxidation states manipulate excited state electronic configurations for constructing highly efficient organic type I photosensitizers†

Jianye Gong,[a] Xiaopeng Wang, [ID] [b] Weijing Zhang,[a] Yifan Wu,[a] Kai Li,[a] Renmanduhu Sha,[a] Lingxiu Liu,[a] Chunbin Li,[a] Lina Feng,[a] Guoyu Jiang [ID] [a] Jianguo Wang [ID] *[a] and Ben Zhong Tang [ID] [c]

The multiple relaxation processes of excited states are a bridge connecting molecular structures and properties, providing enormous application potential for organic luminogens. However, a systematic understanding and manipulation of the relationship between the molecular structure, excited state relaxation processes, and properties of organic luminogens is still lacking. Herein, we report a strategy for manipulating excited state electronic configurations through the regulation of the sulfur oxidation state to construct eminent organic type I PSs. Combined with the experimental results and theoretical calculations, we have successfully revealed the decisive role of high sulfur oxidation states in promoting ROS production capacity. Impressively, a higher sulfur oxidation state can reduce the singlet–triplet energy gap (ΔE_{ST}), increase the matching degree of transition configurations, promote the changes of the excited state electronic configurations, and boost the effective ISC proportion by enhancing intramolecular interactions. Therefore, DBTS2O with the highest sulfur oxidation state exhibits the strongest type I ROS generation ability. Additionally, guided by our strategy, a water-soluble PS (2OA) is designed and synthesized, showing selective imaging capacity and photokilling ability against Gram-positive bacteria. This study broadens the horizons for both molecular design and mechanism study of high-performance organic type I PSs.

Introduction

The relaxation processes of excited organic luminogens include several complex procedures such as vibrational relaxation (VR), internal conversion (IC), intersystem crossing (ISC), reverse intersystem crossing (RISC), fluorescence emission, phosphorescence emission, *etc.*[1–7] These procedures determine the different photophysical behaviors and provide the basis for diverse applications. For decades, regulating the relaxation processes of excited states has become a universal strategy to control the functionality of organic luminogens. For example, manipulating the VR process improved the photothermal conversion efficiency to enhance the photothermal performance of organic phototheranostic agents,[8,9] while promoting

aInner Mongolia Key Laboratory of Fine Organic Synthesis Department, College of Chemistry and Chemical Engineering, Inner Mongolia University, Hohhot 010021, P. R. China. E-mail: wangjg@iccas.ac.cn

*bXi'an Modern Chemistry Research Institute, Xi'an 710069, P. R. China*

cSchool of Science and Engineering, Shenzhen Institute of Aggregate Science and Technology, The Chinese University of Hong Kong, Shenzhen, Shenzhen, Guangdong 518172, P. R. China

† Electronic supplementary information (ESI) available. CCDC 2325250, 2325253 and 2325255. For ESI and crystallographic data in CIF or other electronic format see DOI: https://doi.org/10.1039/d4sc03039g

the ISC process facilitated phosphorescence properties to realize multiple information encryption of organic room temperature phosphorescence (RTP) materials.[10,11] By adjusting the RISC process, efficient organic light-emitting diodes can be achieved.[12,13] Generally, the relaxation processes of excited states are closely related to the molecular structure of organic luminogens.[14–18] Unambiguously, it is significant to comprehensively understand the relaxation processes of excited molecules and to elucidate the structure–activity relationship for developing organic functional luminogens.[19–21]

Photodynamic therapy (PDT) is a modern therapy with non-invasiveness, high specificity, controllable spatio-temporal selectivity and low side effects and shows great potential in clinical applications.[22–24] In recent years, numerous organic luminogens have been successfully developed as photosensitizers (PSs) and applied in PDT due to their good biosafety, easily modifiable structures and excellent fluorescence properties.[25,26] In the PDT process (Scheme 1A), the singlet excited state of PSs (¹PS) undergoes the ISC process to form the triplet excited state of PSs (³PS) after light excitation. Subsequently, ³PS interacts with oxygen through electron transfer (type I) or energy transfer (type II) procedures to generate reactive oxygen species (ROS) which can cause irreversible oxidative damage to biological macromolecules (such as proteins, nucleic acids, lipids, *etc.*).

Therefore, an efficient ISC process is the key to high performance PSs.[27,28] Notably, type I PSs have attracted extensive attention due to their less oxygen-dependent features. Although several design strategies have been reported to improve the ROS production capacity of organic PSs, it is still a huge challenge to construct superior organic type I PSs by enhancing the ISC efficiency.[29] According to the El-Sayed rule (Scheme 1B), the ISC process occurs between excited states with different electronic configurations.[30–32] In other words, the transition from the $^1(n, \pi^*)$ singlet excited state to the $^3(\pi, \pi^*)$ triplet excited state or from the $^1(\pi, \pi^*)$ singlet excited state to the $^3(n, \pi^*)$ triplet excited state is allowed. Therefore, facilitating the transformation of the excited state electronic configurations into an allowed transition mode is an effective method to improve ISC efficiency. However, there are few reports about manipulating the electron configurations of excited states. Additionally, a small singlet-triplet energy gap (ΔE_{ST}) and a similar transition configuration of the excited state are also essential for boosting the ISC process.[33,34] Collectively, these factors need to be fulfilled in the construction of excellent organic PSs. Changing the sulfur oxidation states in sulfides (Scheme 1C) could influence the photophysical properties of molecules by adjusting the relaxation processes of excited states.[35–37] This has been shown to be effective in increasing photoluminescence quantum yields and promoting RTP.[38–43] However, regulating sulfur oxidation states to manipulate excited state electronic configurations for constructing organic type I PSs remains unexplored. Predictably, high sulfur oxidation states can provide the following advantages: (1) strong intramolecular donor–acceptor (D–A) interactions; (2) multiple intermolecular interactions; (3) abundant (n, π^*) electronic configurations. Therefore, it is expected to promote the ISC process by regulating sulfur oxidation states for obtaining brilliant organic type I PSs.

Based on the above discussions, a strategy of manipulating excited state electronic configurations by regulating sulfur oxidation states was proposed to enhance ISC efficiency for constructing organic type I PSs (Scheme 1D). As a proof-of-concept, three D–A–D type (triphenylamine group as a donor and dibenzothiophene group as an acceptor) organic luminogens (DBTS, DBTSO, and DBTS2O) with an aggregation-induced emission (AIE) feature were designed and synthesized by subtly regulating the sulfur oxidation state of the dibenzothiophene group. DBTS, DBTSO, and DBTS2O showed different sulfur oxidation states from sulfide to sulfoxide to sulfone, respectively. Excitedly, DBTS2O exhibited the most redshifted absorption and fluorescence emission as well as the highest type I ROS generation efficiency. Single-crystal analysis indicated that DBTS2O with the highest sulfur oxidation state had abundant intermolecular interactions, implying a compact molecular packing. Theoretical calculations showed that the sulfur oxidation state could significantly affect the electronic configurations of excited states. On one hand, higher sulfur oxidation states enhanced intramolecular D–A interactions, resulting in a smaller ΔE_{ST} and a more similar transition configuration of the excited state. On the other hand, higher sulfur oxidation states changed the proportion of excited state electronic configurations, thus increasing the effective ISC from
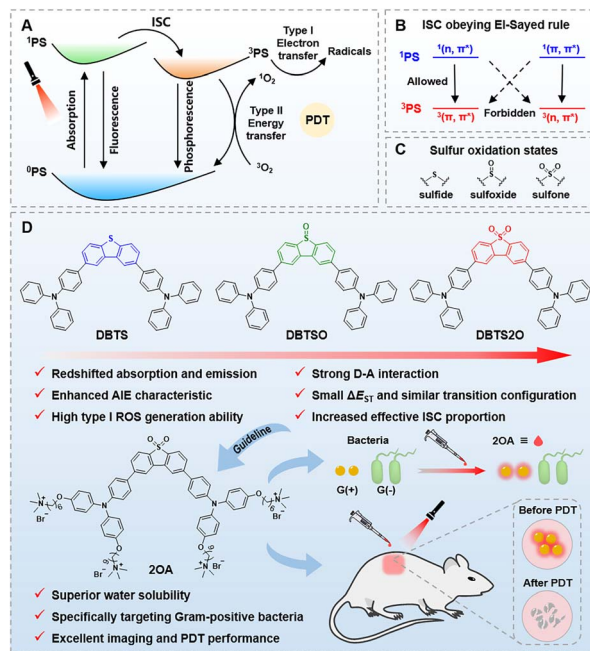

Scheme 1 (A) The mechanism of the PDT process. (B) El-Sayed rule. (C) Different sulfur oxidation states. (D) Schematic diagram of the strategy to enhance ISC efficiency for constructing efficient organic PSs by regulating sulfur oxidation states, and the application of a water-soluble AIE PS (2OA) synthesized according to this strategy for selective imaging and photodynamic killing against Gram-positive bacteria.

$^1(n, \pi^*)$ to $^3(\pi, \pi^*)$ or/and from $^1(\pi, \pi^*)$ to $^3(n, \pi^*)$. These two factors jointly promoted the ISC process of DBTS2O, resulting in its superior type I ROS generation ability. Furthermore, guided by this strategy, an AIE PS (2OA) with good water solubility was synthesized. 2OA showed excellent selective imaging and photodynamic killing against Gram-positive bacteria. Collectively, this study elucidates the structure–activity relationship between the sulfur oxidation state and ROS production capacity, providing valuable insights for the development of efficient organic type I PSs.

Results and discussion

Firstly, DBTS, DBTSO, and DBTS2O with different sulfur oxidation states were synthesized *via* a one-step Suzuki coupling reaction. The detailed synthesis routes and characterization data are provided in the ESI (Schemes S1–S3 and Fig. S1–S12†). The photophysical properties of the three luminogens in DMSO were studied by UV-vis and photoluminescence (PL) spectroscopy. As shown in Fig. 1A, the absorption maxima of DBTS, DBTSO, and DBTS2O peaked at 335, 370, and 375 nm, respectively. And the maximal emission peaks were located at 415, 550, and 564 nm, respectively. DBTS2O showed the most redshifted absorption and emission as well as a 189 nm Stokes shift. The electron cloud distribution of the highest occupied molecular orbitals (HOMOs) and the lowest unoccupied molecular orbitals (LUMOs) for DBTS, DBTSO, and DBTS2O
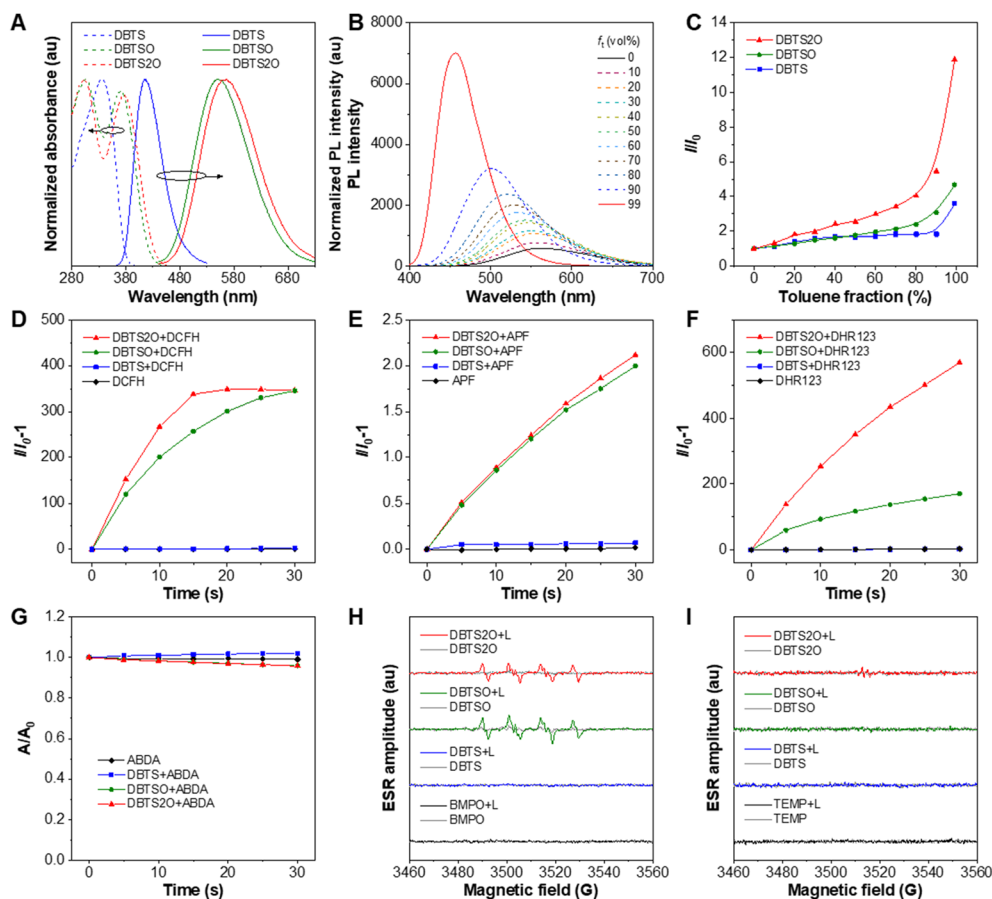
Fig. 1 (A) Normalized absorption spectra (dash line) and PL spectra (solid line) of DBTS, DBTSO, and DBTS2O in DMSO solution (DBTS: $\lambda_{ex} = 330$ nm and DBTSO and DBTS2O: $\lambda_{ex} = 370$ nm). (B) The PL spectra of DBTS2O in DMSO/toluene mixtures with different toluene fractions (f_t). (C) The plot of relative PL intensity of DBTS, DBTSO, and DBTS2O at maximal emission wavelength versus f_t in DMSO/toluene mixtures. ROS generation of DBTS, DBTSO, and DBTS2O after being irradiated with white light: Relative changes in PL intensity of (D) DCFH, (E) APF and (F) DHR 123 and relative changes in absorbance of (G) ABDA in the presence of DBTS, DBTSO, and DBTS2O (5 µM) in DMSO/PBS (v/v, 1/99) upon white light irradiation (100 mW cm^{-2}) for different times. ESR signals of (H) BMPO and (I) TEMP with/without DBTS, DBTSO, and DBTS2O under dark and light conditions.

were calculated using density functional theory (DFT). The HOMOs of the three luminogens were mainly localized on the triphenylamine groups, while the LUMOs were mainly localized on the dibenzothiophene group with different sulfur oxidation states (Fig. S13†). The HOMO–LUMO energy gaps were calculated to be 5.90, 5.48, and 5.35 eV, respectively, indicating a gradual enhancement of intramolecular D–A interactions. Additionally, the AIE properties of DBTS, DBTSO, and DBTS2O were studied in DMSO/toluene mixtures. As depicted in Fig. 1B and C and S14,† the PL intensity of the three luminogens slowly increased as the toluene fraction (f_t) was raised from 0% to 80%. When the toluene fraction reached 99%, the PL intensity of these compounds was obviously enhanced by 3.6-fold, 4.7-fold, and 11.9-fold that in pure DMSO solution, suggesting the typical AIE feature. Moreover, the emissions of DBTS, DBTSO, and DBTS2O were gradually blue-shifted with the increase in f_t due to the twisted intramolecular charge transfer (TICT) effect. Remarkably, DBTS2O showed the strongest AIE properties among the three luminogens. Subsequently, the ROS generation abilities of the three AIE luminogens (AIEgens) were further

investigated under white light irradiation. Initially, dichloro-fluorescein (DCFH) was used as an indicator to detect total ROS production. As shown in Fig. 1D and S15,† after white light irradiation, the PL intensity of DCFH in the presence of DBTS barely showed any change, while the PL intensity of DBTSO + DCFH and DBTS2O + DCFH increased rapidly with prolonged irradiation time. As we expected, the ROS generation efficiency of DBTS2O was higher than that of DBTSO. To confirm the species of ROS, different commercial indicators were used. The ˙OH and O$_2$˙$^-$ generation efficiencies were studied by using aminophenyl fluorescein (APF) and dihydrorhodamine 123 (DHR123) as indicators, respectively. The results were similar to those obtained with DCFH as an indicator. The PL intensity of APF or DHR123 was clearly enhanced in the presence of DBTSO and DBTS2O after white light irradiation, and DBTS2O exhibited superior generation efficiency of ˙OH and O$_2$˙$^-$ (Fig. 1E and F, S16 and S17†). In contrast, no distinct change was observed in DBTS + APF or DBTS + DHR123 solution. When 9,10-anthracenediyl-bis(methylene) dimalonic acid (ABDA) was utilized to assess $^1O_2$, no obvious changes were recorded
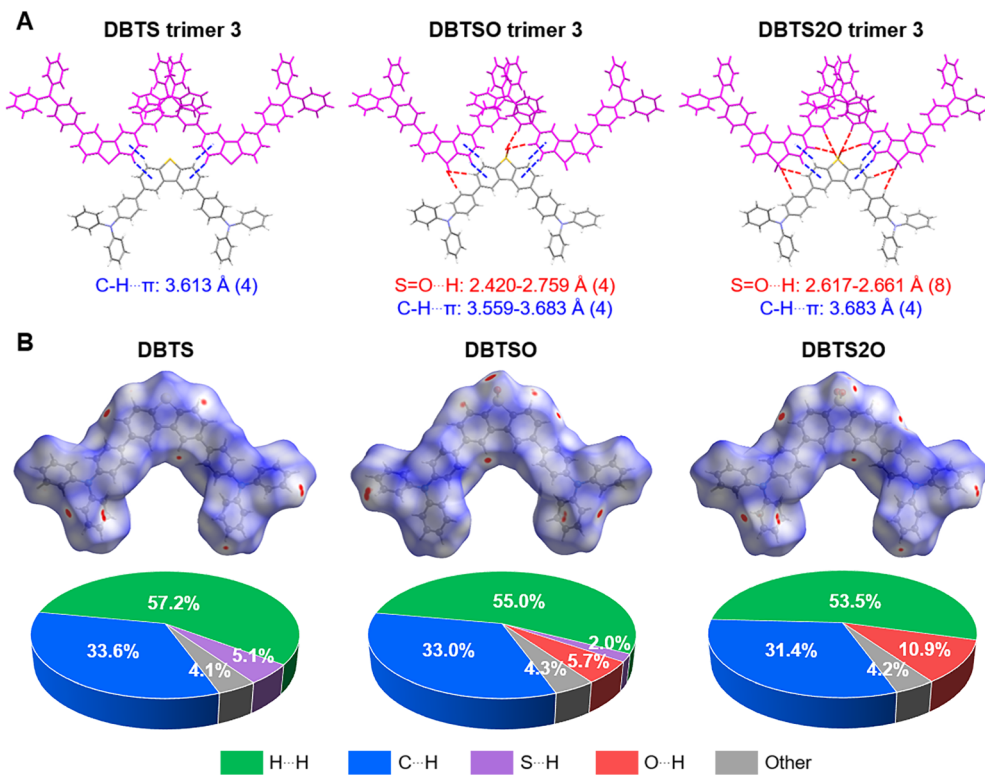
Fig. 2 (A) The intermolecular interactions of trimers in DBTS, DBTSO, and DBTS2O single crystals. (B) Hirshfeld surface analysis and proportions of intermolecular H···H, C···H, S···H, O···H and other interactions to the total intermolecular interactions based on DBTS, DBTSO, and DBTS2O crystal structures.

(Fig. 1G and S18†). These results demonstrated that DBTS2O with the highest sulfur oxidation state had a stronger type I ROS production ability compared to DBTS and DBTSO. In addition, electron spin resonance (ESR) spectroscopy using 5-*tert*-butoxycarbonyl-5-methyl-1-pyrroline-*N*-oxide (BMPO) and 4-amino-2,2,6,6-tetramethylpiperidine (TEMP) as the spin-trap agents was employed to further confirm the generation of free radicals and $^1O_2$. As shown in Fig. 1H, in the presence of BMPO and the three AIEgens, only DBTSO and DBTS2O showed typical ESR signals of free radicals, while DBTS had no ESR signal after white light irradiation. However, no $^1O_2$ ESR signals of the three AIEgens were observed in TEMP-trapping ESR spectra after white light irradiation. These results further verified the type I ROS production ability of DBTSO and DBTS2O.

To understand the mechanism of enhanced ROS production efficiency by a high sulfur oxidation state, single crystal analysis of the three AIEgens was carried out. The single crystals of DBTS (CCDC: 2325250), DBTSO (CCDC: 2325253), and DBTS2O (CCDC: 2325255) were obtained by slow evaporation of ethyl acetate solution (Table S1†). As illustrated in Fig. S19–S21,† the three AIEgens showed similar molecular packing due to the small change of the sulfur oxidation state in molecular structures. The same molecular unit was extracted from the three crystals, which were then separated into three trimers for analysis of intermolecular interactions. In detail, only C–H···π interactions were observed in the three trimers of DBTS. For DBTSO and DBTS2O, however, S=O···H interactions were

gradually observed with the increase in the sulfur oxidation state. Notably, DBTS2O trimers exhibited more S=O···H interactions compared to DBTSO (Fig. 2A). In order to intuitively reflect the difference in intermolecular interactions of DBTS, DBTSO, and DBTS2O, the visualization of intermolecular interactions was conducted based on independent gradient model (IGM) analysis[44,45] using the Multiwfn program[46] and visual molecular dynamics (VMD) program.[47] As shown in Fig. S22–S25,† plentiful green isosurfaces appeared in the DBTS2O trimers, indicating their rich intermolecular interactions. In addition, Hirshfeld surface analysis[48–50] was further performed to quantitatively evaluate the intermolecular interactions of the three AIEgen crystals. Over 90% of total intermolecular interactions were attributed to weak intermolecular C···H, H···H, and other interactions for DBTS, DBTSO, and DBTS2O. As the sulfur oxidation state increased, the ratio of S···H interaction decreased from 5.1% to 2.0% to 0%, while the ratio of O···H interaction increased from 0% to 5.7% to 10.9% (Fig. 2B and S26†). These results suggested that changing the sulfur oxidation state from sulfide to sulfoxide to sulfone effectively strengthened the intermolecular interactions, promoting tight packing in the aggregated state. Moreover, the enhanced O···H interaction also potentially affected the changes in the excited state electron configurations.

To systematically elucidate the structure–activity relationship between high sulfur oxidation states and outstanding ROS production efficiency, theoretical calculations based on the
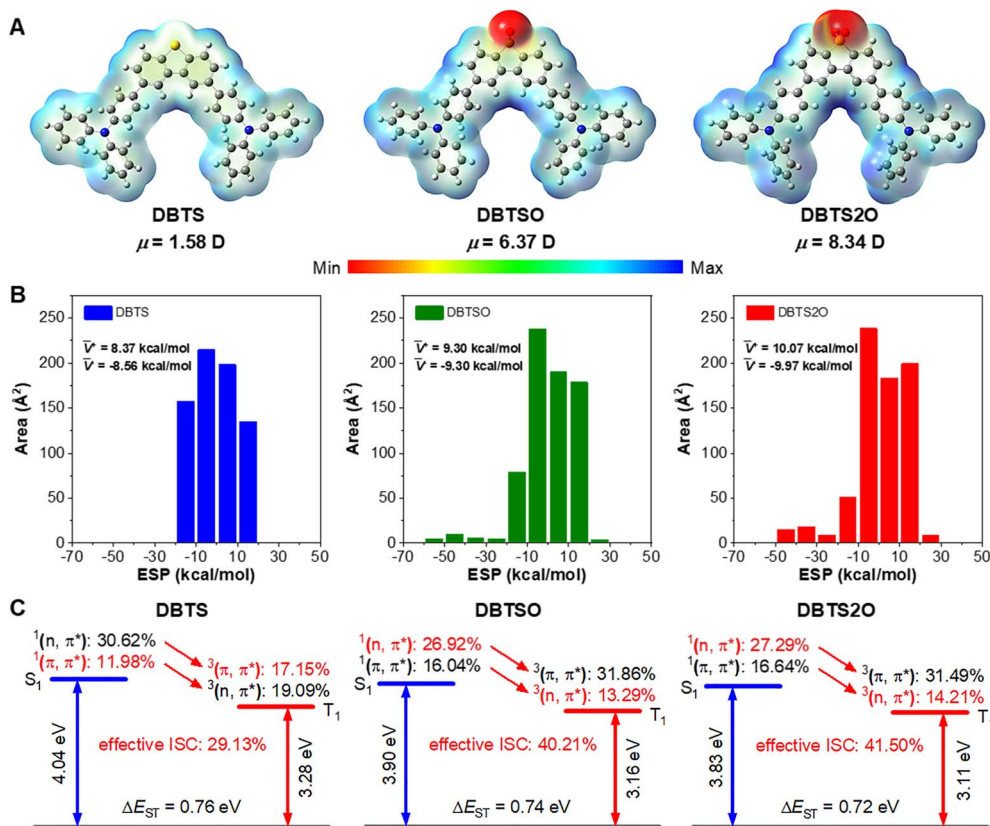
Fig. 3 The theoretical calculation results of DBTS, DBTSO, and DBTS2O. (A) ESP distributions and dipole moment (μ). (B) The histograms of electrostatic potential area distribution, positive average ESP value ($\bar{V}^+$) and negative average ESP value ($\bar{V}^-$). (C) Calculated energy levels of S_1 and T_1 states, and the proportions of $^1(n, \pi^*)$, $^3(n, \pi^*)$, $^1(\pi, \pi^*)$ and $^3(\pi, \pi^*)$.

crystal structure were carried out. The electrostatic potential (ESP) distributions[51–54] of DBTS, DBTSO, and DBTS2O are displayed in Fig. 3A. Notably, the acceptor of DBTS had weak electron-withdrawing properties, and there was no significant difference in ESP between the donor and acceptor. When the sulfur atom of the dibenzothiophene group was oxidized, the strong electronegativity of the oxygen atom enhanced the local electron-withdrawing properties, resulting in a more negative ESP for the sulfoxide and sulfone parts of DBTSO and DBTS2O. Meanwhile, the molecular dipole moment gradually increased. DBTS2O with the highest sulfur oxidation state showed the largest molecular dipole moment of 8.34 D, indicating its strong intramolecular D–A interaction. Furthermore, in order to gain a deeper understanding of the ESP differences among the three AIEgens, the surface areas of ESP were also analyzed. DBTS2O had a larger surface area with ESP values of −45, −35, −25, 15, and 25 kcal mol^{-1}, while it had a smaller area at −15 and 5 kcal mol^{-1} than DBTS and DBTSO (Fig. 3B). The positive average ESP value ($\bar{V}^+$) and the negative average ESP value ($\bar{V}^-$) of DBTS2O were calculated to be 10.07 and −9.97 kcal mol^{-1}, respectively. These results not only demonstrated that the change in the sulfur oxidation state significantly affected the strength of D–A interaction, but also further illustrated the strongest D–A interaction of DBTS2O. Subsequently, the electronic configurations of excited states for the three AIEgens were studied

using time-dependent density functional theory (TD-DFT). As shown in Fig. 3C, the energy levels of the first singlet excited state (S_1) and the first triplet excited state (T_1) for DBTS, DBTSO, and DBTS2O gradually decreased with the enhancement of intramolecular D–A interactions. The calculated ΔE_{ST} of DBTS, DBTSO, and DBTS2O were 0.76, 0.74, and 0.72 eV, respectively. Meanwhile, the transition configurations of S_1 and T_1 also changed from H → L+1 to H → L, and the matching degree gradually increased (Fig. S27–S29 and Table S2†). The smaller ΔE_{ST} and the more similar transition configuration of the excited state suggested that the increase in the sulfur oxidation state could promote the ISC process by enhancing intramolecular D–A interactions. More importantly, according to the El-Sayed rule, the ISC process from $^1(n, \pi^*)$ to $^3(\pi, \pi^*)$ or from $^1(\pi, \pi^*)$ to $^3(n, \pi^*)$ is favored. Thus, the electronic configurations of the excited states for DBTS, DBTSO, and DBTS2O were studied to assess transition modes by using natural transition orbital (NTO) analysis. Considering the proportion difference in different electron configurations, the type of electron configuration with a smaller proportion in the allowed transition mode was used to determine the effective transition. The proportion sum of the two effective transition modes was the final effective ISC proportion. The effective ISC proportions of DBTS, DBTSO, and DBTS2O were calculated to be 29.13%, 40.21%, and 41.50%, respectively, indicating that DBTS2O underwent the
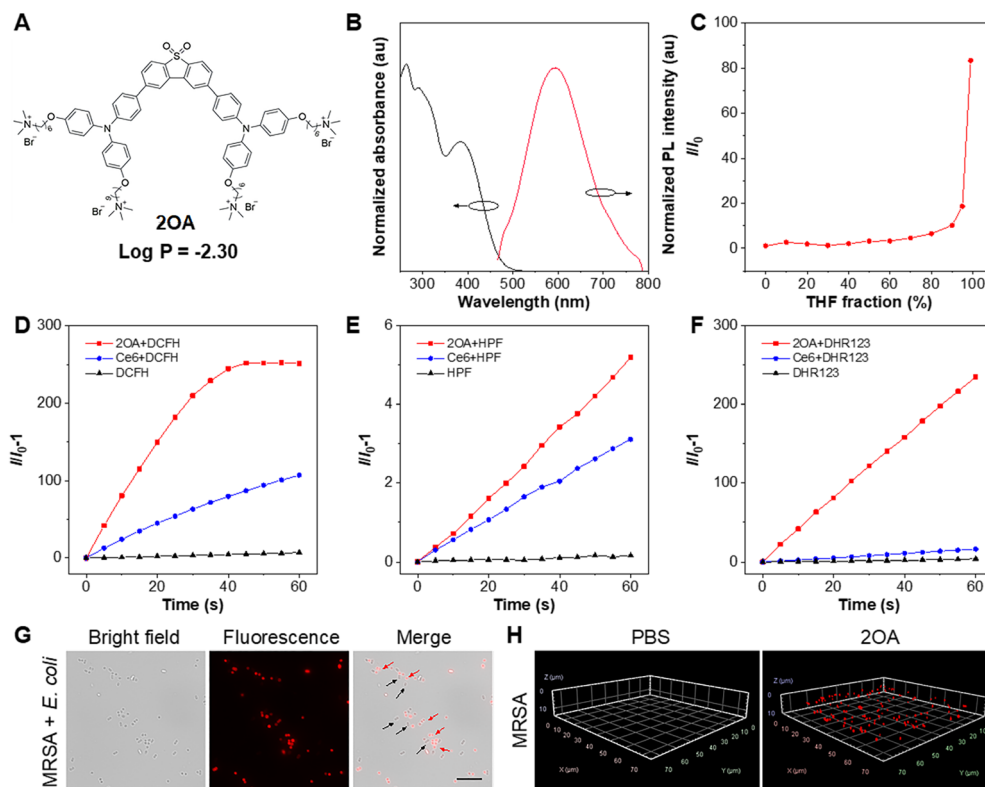
Fig. 4 (A) The molecular structure and lipid–water partition coefficient of 2OA. (B) Normalized absorption spectra and fluorescence spectra of 2OA in aqueous solution (λ_{ex} = 400 nm). (C) The plot of relative PL intensity of 2OA at the maximum emission wavelength *versus* the THF fraction in water/THF mixtures. ROS generation of 2OA after being irradiated with white light: relative changes in PL intensity of (D) DCFH, (E) HPF and (F) DHR 123 in the presence of 2OA (5 μM) in PBS upon white light irradiation (8 mW cm^{-2}) for different times. (G) Bright-field and fluorescent images of an MRSA + *E. coli* mixture incubated with 2OA (5 μM). The black arrows represent *E. coli* and the red arrows represent MRSA. Scar bar = 10 μm. (H) The 3D CLSM images of MRSA incubated with 2OA (5 μM).

most efficient ISC process among the three AIEgens (Fig. 3C). The NTOs of excited states and the calculated details of electron configuration proportions for the three AIEgens are displayed in Fig. S30–S32 and Tables S3–S5.† Collectively, by increasing the sulfur oxidation state, the intramolecular D–A interaction could be significantly enhanced, resulting in a reduced ΔE_{ST}, an increased matching degree of transition configurations, changes in the excited state electronic configurations and a higher effective ISC proportion, which ultimately improved ROS generation efficiency. These results clearly elucidated the structure–activity relationship between high sulfur oxidation states and superior ROS production efficiency.

As mentioned above, the ROS production efficiency of organic photosensitizers could be effectively enhanced by adjusting the sulfur oxidation state. According to our strategy, a cationic derivative of DBTS2O, namely 2OA, was designed and synthesized (Scheme S4 and Fig. S33–S40†). Notably, the lipid–water partition coefficient of 2OA was −2.30, indicating its excellent water solubility (Fig. 4A), which is favorable for biological applications.[55–57] Therefore, the optical properties of 2OA were evaluated in aqueous solution. 2OA showed a maximal absorption at 386 nm and an emission maximum at 593 nm (Fig. 4B). The Stokes shift reached 207 nm, which effectively avoids the interference of the excitation light and is suitable for

fluorescence imaging applications.[58–60] Subsequently, the AIE characteristic of 2OA was investigated in a water/THF mixture with THF as a poor solvent due to the excellent water solubility of 2OA. 2OA had almost no emission in aqueous solution and showed 83-fold emission enhancement in a 99% THF fraction, indicating its AIE characteristic (Fig. 4C and S41†). The ROS generation abilities of 2OA were further tested. Different indicators, DCFH, hydroxyphenyl fluorescein (HPF), and DHR123, were employed to detect ROS production ability. Chlorin e6 (Ce6) was used as a reference. As expected, Fig. 4D and E and S42–S44† show that 2OA exhibited a higher efficiency in ROS production compared to Ce6 under different indicator conditions. However, the $^{1}O_{2}$ production efficiency of Ce6 was higher than that of 2OA (Fig. S45†). These results confirmed that 2OA was a highly efficient PS, primarily generating type I ROS.

The annual death toll from antimicrobial resistance is on the rise, with projections indicating a staggering 10 million fatalities globally by 2050.[61,62] This alarming trend poses a significant risk to both human health and public health security.[63–65] PDT has been recognized as an effective method for treating drug-resistant bacterial infections due to its unique killing mechanism and its ability to prevent antimicrobial resistance.[66–69] 2OA not only had excellent photophysical properties and ROS production ability, but also positive charges that were
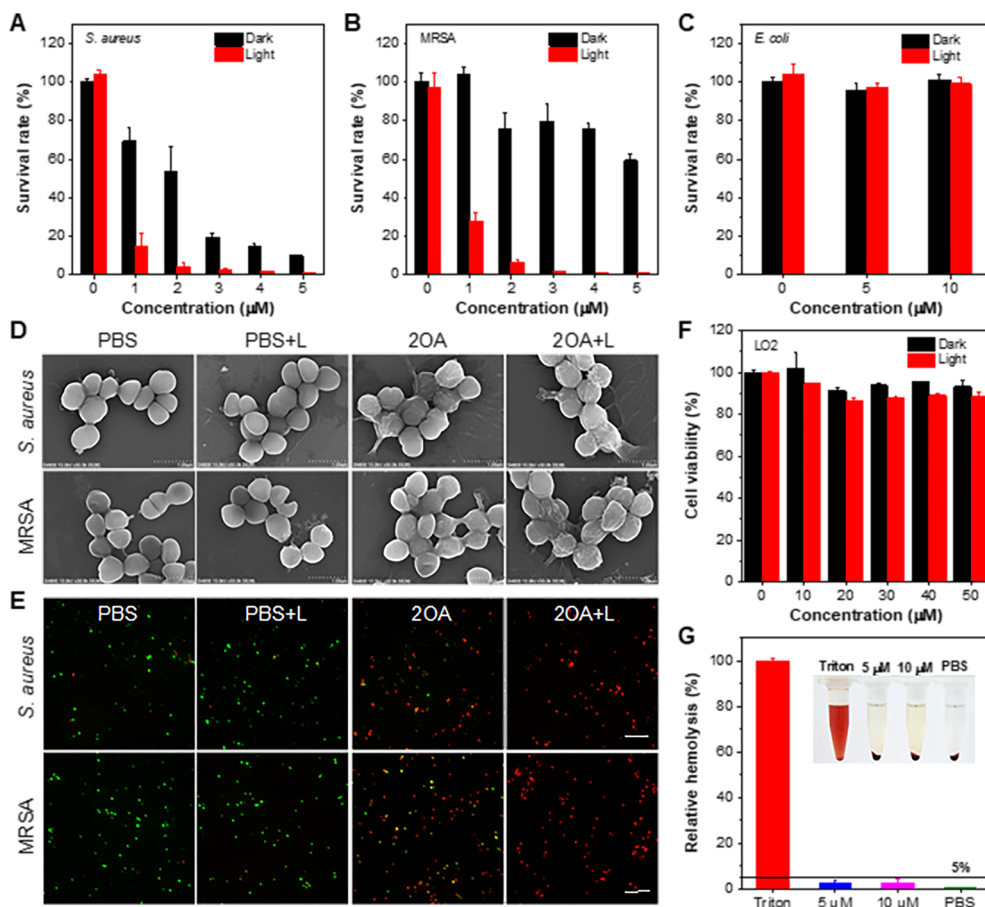
Fig. 5 Bacterial killing efficiency of (A) *S. aureus*, (B) MRSA and (C) *E. coli* incubated with 2OA at different concentrations with/without white light irradiation. (D) SEM images of *S. aureus* and MRSA treated with PBS or 2OA (5 μM) with/without white light irradiation. (E) Live/dead bacterial staining images of *S. aureus* and MRSA treated with PBS or 2OA (5 μM) with/without white light irradiation. Green channel: calcein–AM. Red channel: propidium iodide. Scar bar = 20 μm. (F) Cell viability of LO2 cells incubated with various concentrations of 2OA with/without white light irradiation. (G) Hemolysis rates of 2OA. Triton and PBS were used as the positive control and negative control, respectively. Inset: the photographs of hemolytic activity.

conducive to binding with the negatively charged surfaces of bacteria. Therefore, 2OA was expected to be applied for imaging and photodynamic killing of drug-resistant bacteria. Gram-positive bacteria *S. aureus*, methicillin-resistant *S. aureus* (MRSA) and Gram-negative bacteria *E. coli* were selected as representative bacteria. In the preliminary bacterial imaging experiment, stark fluorescent signals were clearly observed in *S. aureus* and MRSA after being incubated with 2OA (Fig. S46†). However, the fluorescence emission in *E. coli* was barely visible. This could be attributed to the dense outer membrane structure of Gram-negative bacteria, which provides enormous obstacles to drug binding. These results were consistent with the changes in PL spectra before and after incubating 2OA with bacteria (Fig. S47†). Subsequently, *S. aureus* and MRSA were co-cultured with *E. coli* respectively under the same conditions and then incubated with 2OA. Interestingly, as shown in Fig. 4G and S48,† *S. aureus* and MRSA were selectively lit-up, while *E. coli* showed a low fluorescent signal. And the fluorescence intensity ratios were 5.3-fold and 6.7-fold, respectively (Fig. S49†). These results solidly suggested the brilliant performance of 2OA for

accurate discrimination of Gram-positive bacteria. Moreover, 2OA had the ability to perform 3D imaging on *S. aureus* and MRSA with a high signal-to-noise ratio (Fig. 4H and S50†). To further verify the selective binding capacity of 2OA for Gram-positive bacteria, the changes in zeta potential (ξ) of *S. aureus*, MRSA, and *E. coli* before and after incubation with 2OA were studied. As depicted in Table S6,† the ξ values of both *S. aureus* and MRSA showed a positive shift after incubation with 2OA, while the ξ value of *E. coli* remained almost unchanged. These data provided further evidence of effective binding between 2OA and Gram-positive bacteria.

Encouraged by its selective imaging capacity and excellent ROS production ability, the photodynamic antibacterial performance of 2OA was investigated through the plate count method. As shown in Fig. 5A–C and S51,† 2OA at 5 μM was able to eliminate more than 99% of *S. aureus* and MRSA upon white light irradiation. However, although the concentration of 2OA was increased to 10 μM, the survival rate of *E. coli* remained unchanged under light conditions. These data indicated the specific killing ability of 2OA against Gram-positive bacteria.
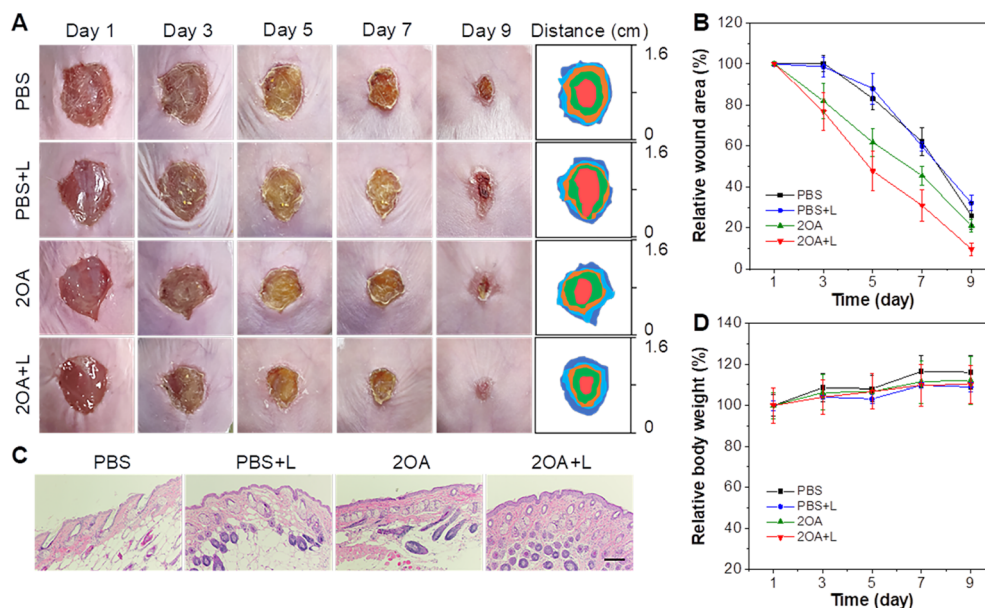
Fig. 6 (A) Photographs of the MRSA-infected wounds after different treatments on days 1, 3, 5, 7, and 9 and the scale bars (on the right). (B) The diagrams of the relative wound area during the wound healing process after different treatments. Error bar: mean $\pm$ SD ($n = 4$). (C) H&E staining images of wound tissues at day 9 after different treatments. Scar bar = 50 μm. (D) The diagrams of relative body weight during the wound healing process after different treatments. Error bar: mean $\pm$ SD ($n = 4$).

Subsequently, to evaluate the bacteriostatic process of 2OA in detail, the growth curves of *S. aureus*, MRSA and *E. coli* in the presence of 2OA with varying concentrations were monitored for 10 h. As shown in Fig. S52,† the 90% minimum inhibitory concentration (MIC_{90}) values of 2OA against *S. aureus* and MRSA under light conditions were as low as 6.54 μM and 6.56 μM, respectively, further indicating that 2OA had an outstanding photodynamic killing effect on Gram-positive bacteria, including drug-resistant bacteria. The scanning electron microscopy (SEM) analysis results showed that the smooth membrane surfaces of *S. aureus* and MRSA were vigorously crumpled and collapsed after treatment with 2OA under white light irradiation, resulting in bacterial death (Fig. 5D). Moreover, we also visualized the antibacterial effect of 2OA by live/dead fluorescent staining. In comparison to the control group in the absence of 2OA, obvious red fluorescence, a marker of bacterial death, was observed in the presence of 2OA for both *S. aureus* and MRSA, particularly after being irradiated with white light (Fig. 5E, S53 and S54†). These data were in good agreement with the results of the *in vitro* antibacterial experiments. Good biocompatibility is another key parameter to evaluate the performance of PSs. Therefore, the cytotoxicity of 2OA toward LO2 cells was assessed by MTT assay. As shown in Fig. 5F, 2OA demonstrated negligible toxicity toward LO2 cells with an increasing concentration of 50 μM under both dark and light conditions. Furthermore, the blood compatibility of 2OA was also evaluated through a hemolysis experiment. The hemolysis analysis shown in Fig. 5G suggested that 2OA had excellent blood compatibility even at a high concentration of 10 μM. These results systematically showed the good biocompatibility of 2OA.

Combining the results of the *in vitro* antibacterial experiments and the biocompatibility assessments, we further evaluated the antibacterial activity of 2OA *in vivo*. An animal model with MRSA-infected wounds was established on the dorsal skin of mice. The mice were randomly divided into four groups, including PBS only (PBS group), PBS with white light irradiation (PBS + L group), 2OA only (2OA group), and 2OA with white light irradiation (2OA + L group). The photographs of the wounds during the healing process were recorded. As shown in Fig. 6A and B, the 2OA + L group maintained a faster rate of wound healing from day 3 onwards compared to the other groups. By day 9, the wounds in the 2OA + L group were almost completely healed, while the other groups still showed visible scabs. The hematoxylin and eosin (H&E) staining of wound tissue on day 9 showed that the epidermal and dermal layers of the wound tissue in the 2OA + L group were intact and thick, indicating better wound healing (Fig. 6C). Therefore, the *in vivo* experiments sufficiently demonstrated that 2OA could effectively treat wound infections caused by MRSA. In addition, the biosafety of 2OA was further assessed in the process of animal experiments. As depicted in Fig. S55 and S56,† the parameters of blood routine and blood biochemistry analysis for liver and kidney functions were within the normal range. Meanwhile, no obvious damage was found in all organs of the mice treated with 2OA (Fig. S57†). Besides, the body weight of the mice in each group showed minimal changes during the treatment process (Fig. 6D). These results powerfully evidenced the excellent biosafety of 2OA.

Conclusions

In summary, we proposed a facile strategy involving the manipulation of excited state electronic configurations using sulfur

oxidation states to construct highly efficient organic type I PSs. Three D–A–D type AIEgens, DBTS, DBTSO, and DBTS2O, were designed and synthesized with different sulfur oxidation states. Therein, DBTS2O showed the most redshifted optical properties and the highest type I ROS generation efficiency. Notably, theoretical calculations uncovered deeper origins. A high sulfur oxidation state could significantly affect the electronic configurations of excited states by enhancing intramolecular D–A interactions. Higher sulfur oxidation states not only reduced ΔE_{ST} and increased the matching degree of transition configurations, but also increased the proportion of effective ISC, resulting in the excellent ROS generation ability of DBTS2O. According to this strategy, a highly water-soluble AIE PS (2OA) was synthesized. 2OA could selectively bind Gram-positive bacteria and provide high signal-to-noise ratio imaging. Moreover, the outstanding photo-killing efficacy against Gram-positive bacteria *in vitro* and favorable biocompatibility have promoted the effective use of 2OA for treating MRSA-infected wounds. This work not only elucidates the structure–activity relationship of enhanced type I ROS production capacity caused by a high sulfur oxidation state, but also successfully develops a water-soluble AIE PS against Gram-positive bacteria guided by this strategy, which provides new ideas for the development of efficient organic type I PSs.

Data availability

All data (experimental procedures and characterization) that support the findings of this study are available within the article and its ESI. Crystallographic data for DBTS, DBTSO, and DBTS2O have been deposited at the Cambridge Structural Database (CSD) of the Cambridge Crystallographic Data Centre (CCDC) with the CCDC numbers 2325250, 2325253, and 2325255 on the CSD website (**https://www.ccdc.cam.ac.uk/**).†

Author contributions

Guoyu Jiang, Jianguo Wang and Ben Zhong Tang contributed to the conceptualization and supervision. Jianye Gong, Xiaopeng Wang, Weijing Zhang, Yifan Wu, Kai Li, Renmanduhu Sha, Lingxiu Liu, Chunbin Li and Lina Feng contributed to the methodology. Jianye Gong and Weijing Zhang contributed to the software. Jianye Gong, Guoyu Jiang and Jianguo Wang contributed to the original draft writing. Jianye Gong, Guoyu Jiang, Jianguo Wang and Ben Zhong Tang contributed to the review & editing.

Conflicts of interest

There are no conflicts to declare.

Acknowledgements

Notes and references

1 K. Chen, Y. Zhang, Y. Lei, W. Dai, M. Liu, Z. Cai, H. Wu, X. Huang and X. Ma, *Nat. Commun.*, 2024, **15**, 1269.

2 W. Dai, Y. Jiang, Y. Lei, X. Huang, P. Sun, J. Shi, B. Tong, D. Yan, Z. Cai and Y. Dong, *Chem. Sci.*, 2024, **15**, 4222–4237.

3 H. Deng, G. Li, H. Xie, Z. Yang, Z. Mao, J. Zhao, Z. Yang, Y. Zhang and Z. Chi, *Angew. Chem., Int. Ed.*, 2024, **63**, e202317631.

4 Kenry, C. Chen and B. Liu, *Nat. Commun.*, 2019, **10**, 2111.

5 V.-N. Nguyen, Z. Zhao, B. Z. Tang and J. Yoon, *Chem. Soc. Rev.*, 2022, **51**, 3324–3340.

6 P. Wang, B. Wu, M. Li, Y. Song, C. Chen, G. Feng, D. Mao, F. Hu and B. Liu, *ACS Nano*, 2023, **17**, 10365–10375.

7 G. Jiang, J. Yu, J. Wang and B. Z. Tang, *Aggregate*, 2022, **3**, e285.

8 C. Li, G. Jiang, J. Yu, W. Ji, L. Liu, P. Zhang, J. Du, C. Zhan, J. Wang and B. Z. Tang, *Adv. Mater.*, 2023, **35**, e2208229.

9 M. Zheng, Q. Yang, C. Lu, X. Wu, W. Yan and D. Liu, *Drug Discovery Today*, 2023, **28**, 103598.

10 M. Gao, J. Ren, Y. Gong, M. Fang, J. Yang and Z. Li, *Aggregate*, 2024, **5**, e462.

11 F. Xiao, H. Gao, Y. Lei, W. Dai, M. Liu, X. Zheng, Z. Cai, X. Huang, H. Wu and D. Ding, *Nat. Commun.*, 2022, **13**, 186.

12 J. Fang, Z. Liu, J. Li, N. Zhuang, D. Yang, D. Ma, B. Z. Tang and Z. Zhao, *Adv. Opt. Mater.*, 2023, **11**, 2300835.

13 Y. Xiao, H. Wang, Z. Xie, M. Shen, R. Huang, Y. Miao, G. Liu, T. Yu and W. Huang, *Chem. Sci.*, 2022, **13**, 8906–8923.

14 Y. Liu, M. Gu, Q. Ding, Z. Zhang, W. Gong, Y. Yuan, X. Miao, H. Ma, X. Hong, W. Hu and Y. Xiao, *Angew. Chem., Int. Ed.*, 2023, **62**, e202214875.

15 J. Sun and X. He, *Aggregate*, 2022, **3**, e282.

16 S. Yang, J. Zhang, Z. Zhang, R. Zhang, X. Ou, W. Xu, M. Kang, X. Li, D. Yan, R. T. K. Kwok, J. Sun, J. W. Y. Lam, D. Wang and B. Z. Tang, *J. Am. Chem. Soc.*, 2023, **145**, 22776–22787.

17 Y. Yang, Q. Jiang and F. Zhang, *Chem. Rev.*, 2023, **124**, 554–628.

18 D. Zhang, C. Li, G. Zhang, J. Tian and Z. Liu, *Acc. Chem. Res.*, 2024, **57**, 625–635.

19 J. Gong, L. Liu, C. Li, Y. He, J. Yu, Y. Zhang, L. Feng, G. Jiang, J. Wang and B. Z. Tang, *Chem. Sci.*, 2023, **14**, 4863–4871.

20 J. Guo, J. Dai, X. Peng, Q. Wang, S. Wang, X. Lou, F. Xia, Z. Zhao and B. Z. Tang, *ACS Nano*, 2021, **15**, 20042–20055.

21 R.-N. Su, Q.-Q. Pan, G.-Y. Ding, J. Sun, L.-L. Wen, K.-Z. Shao, S.-B. Wang, G.-G. Shan and Z.-M. Su, *J. Mater. Chem. C*, 2023, **11**, 9908–9915.

22 C. Li, J. Liu, Y. Hong, R. Lin, Z. Liu, M. Chen, J. W. Y. Lam, G. H. Ning, X. Zheng, A. Qin and B. Z. Tang, *Angew. Chem., Int. Ed.*, 2022, **61**, e202202005.

23 K. X. Teng, D. Zhang, B. K. Liu, Z. F. Liu, L. Y. Niu and Q. Z. Yang, *Angew. Chem., Int. Ed.*, 2024, **63**, e202318783.

24 G. Zhang, X. Chen, X. Chen, K. Du, K. Ding, D. He, D. Ding, R. Hu, A. Qin and B. Z. Tang, *ACS Nano*, 2023, **17**, 14800–14813.

25 Y. Wu, J. Li, Z. Shen, D. Wang, R. Dong, J. Zhang, Y. Pan, Y. Li, D. Wang and B. Z. Tang, *Angew. Chem., Int. Ed.*, 2022, **61**, e202212386.

26 G. Yang, J. S. Ni, Y. Li, M. Zha, Y. Tu and K. Li, *Angew. Chem., Int. Ed.*, 2021, **60**, 5386–5393.

27 Z. Zhang, M. Kang, H. Tan, N. Song, M. Li, P. Xiao, D. Yan, L. Zhang, D. Wang and B. Z. Tang, *Chem. Soc. Rev.*, 2022, **51**, 1983–2030.

28 Q. Wang, C. Li, Y. Song, Q. Shi, H. Li, H. Zhong, J. Wang and F. Hu, *Chem. Sci.*, 2023, **14**, 684–690.

29 T. C. Pham, V.-N. Nguyen, Y. Choi, S. Lee and J. Yoon, *Chem. Rev.*, 2021, **121**, 13454–13619.

30 H. Ma, Q. Peng, Z. An, W. Huang and Z. Shuai, *J. Am. Chem. Soc.*, 2018, **141**, 1010–1015.

31 Z. Xu, Y. He, H. Shi and Z. An, *SmartMat*, 2022, **4**, e1139.

32 W. Zhao, Z. He, J. W. Y. Lam, Q. Peng, H. Ma, Z. Shuai, G. Bai, J. Hao and B. Z. Tang, *Chem*, 2016, **1**, 592–602.

33 Z. An, C. Zheng, Y. Tao, R. Chen, H. Shi, T. Chen, Z. Wang, H. Li, R. Deng, X. Liu and W. Huang, *Nat. Mater.*, 2015, **14**, 685–690.

34 J. Yu, H. Ma, W. Huang, Z. Liang, K. Zhou, A. Lv, X.-G. Li and Z. He, *JACS Au*, 2021, **1**, 1694–1699.

35 C. D. Cruz, P. R. Christensen, E. L. Chronister, D. Casanova, M. O. Wolf and C. J. Bardeen, *J. Am. Chem. Soc.*, 2015, **137**, 12552–12564.

36 E. Varathan and A. Patnaik, *J. Phys. Chem. A*, 2019, **123**, 8755–8765.

37 J. Yuan, Z. Xu and M. O. Wolf, *Chem. Sci.*, 2022, **13**, 5447–5464.

38 P. R. Christensen, J. K. Nagle, A. Bhatti and M. O. Wolf, *J. Am. Chem. Soc.*, 2013, **135**, 8109–8112.

39 K.-M. Tong, J. Toigo, B. O. Patrick and M. O. Wolf, *Inorg. Chem.*, 2023, **62**, 13662–13671.

40 K. Yamamoto, W. Imai, S. Kanamori, K. Yamamoto and Y. Nakamura, *J. Org. Chem.*, 2023, **88**, 4003–4007.

41 J. Yuan, L. Jiang, T. Nishimura, E. R. Sauvé, D. Hean, K. Maeda and M. O. Wolf, *J. Org. Chem.*, 2022, **87**, 12315–12322.

42 Y. Wen, H. Liu, S.-T. Zhang, G. Pan, Z. Yang, T. Lu, B. Li, J. Cao and B. Yang, *CCS Chem.*, 2021, **3**, 1940–1948.

43 Z. Xu, C. Climent, C. M. Brown, D. Hean, C. J. Bardeen, D. Casanova and M. O. Wolf, *Chem. Sci.*, 2021, **12**, 188–195.

44 C. Lefebvre, G. Rubez, H. Khartabil, J. C. Boisson, J. Contreras-Garcia and E. Henon, *Phys. Chem. Chem. Phys.*, 2017, **19**, 17928–17936.

45 T. Lu and Q. Chen, *J. Comput. Chem.*, 2022, **43**, 539–555.

46 T. Lu and F. Chen, *J. Comput. Chem.*, 2012, **33**, 580–592.

47 W. Humphrey, A. Dalke and K. Schulten, *J. Mol. Graphics*, 1996, **14**, 33–38.

48 M. A. Spackman and D. Jayatilaka, *CrystEngComm*, 2009, **11**, 19–32.

49 M. A. Spackman and J. J. McKinnon, *CrystEngComm*, 2002, **4**, 378–392.

50 P. R. Spackman, M. J. Turner, J. J. McKinnon, S. K. Wolff, D. J. Grimwood, D. Jayatilaka and M. A. Spackman, *J. Appl. Crystallogr.*, 2021, **54**, 1006–1011.

51 H. Yao, Y. Cui, D. Qian, C. S. Ponseca, A. Honarfar, Y. Xu, J. Xin, Z. Chen, L. Hong, B. Gao, R. Yu, Y. Zu, W. Ma, P. Chabera, T. Pullerits, A. Yartsev, F. Gao and J. Hou, *J. Am. Chem. Soc.*, 2019, **141**, 7743–7750.

52 T. Lu and Q. Chen, *J. Mol. Model.*, 2020, **26**, 315.

53 J. Zhang and T. Lu, *Phys. Chem. Chem. Phys.*, 2021, **23**, 20323–20328.

54 Y. Cui, P. Zhu, H. Hu, X. Xia, X. Lu, S. Yu, H. Tempeld, R. A. Eichel, X. Liao and Y. Chen, *Angew. Chem., Int. Ed.*, 2023, **62**, e202304931.

55 L. Liu, C. Li, J. Gong, Y. Zhang, W. Ji, L. Feng, G. Jiang, J. Wang and B. Z. Tang, *Angew. Chem., Int. Ed.*, 2023, **62**, e202307776.

56 A. Ji, H. Lou, C. Qu, W. Lu, Y. Hao, J. Li, Y. Wu, T. Chang, H. Chen and Z. Cheng, *Nat. Commun.*, 2022, **13**, 3815.

57 C. Zhou, Z. Li, Z. Zhu, G. W. N. Chia, A. Mikhailovsky, R. J. Vázquez, S. J. W. Chan, K. Li, B. Liu and G. C. Bazan, *Adv. Mater.*, 2022, **34**, 2201989.

58 L. Feng, C. Li, L. Liu, X. Chen, G. Jiang, J. Wang and B. Z. Tang, *Angew. Chem., Int. Ed.*, 2023, **62**, e202212673.

59 C.-J. Wu, X.-Y. Li, T. Zhu, M. Zhao, Z. Song, S. Li, G.-G. Shan and G. Niu, *Anal. Chem.*, 2022, **94**, 3881–3887.

60 J. Liu, W. Zhang, X. Wang, Q. Ding, C. Wu, W. Zhang, L. Wu, T. D. James, P. Li and B. Tang, *J. Am. Chem. Soc.*, 2023, **145**, 19662–19675.

61 J. Li, G. Pan, G. V. Zyryanov, Y. Peng, G. Zhang, L. Ma, S. Li, P. Chen and Z. Wang, *ACS Appl. Mater. Interfaces*, 2023, **15**, 40864–40876.

62 P. Xiao, Z. Shen, D. Wang, Y. Pan, Y. Li, J. Gong, L. Wang, D. Wang and B. Z. Tang, *Adv. Sci.*, 2021, **9**, 2104079.

63 Z. Pang, N. Ren, Y. Wu, J. Qi, F. Hu, Y. Guo, Y. Xie, D. Zhou and X. Jiang, *Adv. Mater.*, 2023, **35**, 2303562.

64 S. Shen, Y. Huang, A. Yuan, F. Lv, L. Liu and S. Wang, *CCS Chem.*, 2021, **3**, 129–135.

65 T. Li, Y. Wu, W. Cai, D. Wang, C. Ren, T. Shen, D. Yu, S. Qiang, C. Hu, Z. Zhao, J. Yu, C. Peng and B. Z. Tang, *Adv. Sci.*, 2022, **9**, 2202485.

66 Q. Guo, S. Xue, J. Feng, C. Peng, C. Zhou and Y. Qiao, *Adv. Healthcare Mater.*, 2023, **12**, 2300818.

67 Q. Li, Y. Li, T. Min, J. Gong, L. Du, D. L. Phillips, J. Liu, J. W. Y. Lam, H. H. Y. Sung, I. D. Williams, R. T. K. Kwok, C. L. Ho, K. Li, J. Wang and B. Z. Tang, *Angew. Chem., Int. Ed.*, 2019, **59**, 9470–9477.

68 X. Wu, M. Yang, J. S. Kim, R. Wang, G. Kim, J. Ha, H. Kim, Y. Cho, K. T. Nam and J. Yoon, *Angew. Chem., Int. Ed.*, 2022, **61**, e202200808.

69 E. Y. Yu, J. H. C. Chau, M. M. S. Lee, T. H. Koo, R. Lortz, J. W. Y. Lam, R. T. K. Kwok, Y. Li and B. Z. Tang, *ACS Nano*, 2024, **18**, 1907–1920.